

Optimizing Quantum Chemistry Simulations with a Hybrid Quantization Scheme

Calvin Ku,^{1,2} Yu-Cheng Chen,^{2,1,*} Alice Hu,^{1,3,†} and Min-Hsiu Hsieh^{2,‡}

¹*Department of Mechanical Engineering, City University of Hong Kong, Kowloon, Hong Kong SAR 999077, China*

²*Hon Hai Research Institute, Taipei, Taiwan*

³*Department of Material Science and Engineering, City University of Hong Kong, Kowloon, Hong Kong SAR 999077, China*

Unlike classical algorithms, where second quantization is ubiquitous, the nature of quantum computers enables both the first- and second-quantized representations to be on somewhat equal footing. While quantum algorithms of both quantizations provide advantages over classical algorithms for ground state calculation and time-evolution, they face distinct limitations and inefficiencies in addressing real-world molecular and material simulation problems. As an example, the first-quantized representation is unsuitable for calculating electron non-conserving properties, such as dynamic correlations. Conversely, the ground-state molecular orbital wavefunction efficiently prepared in the second quantization may benefit from efficient first-quantized measurement circuits. In light of this, we propose a hybrid quantization scheme for electronic simulations that employs a conversion circuit to switch efficiently between the two quantizations, achieving a gate cost of $\mathcal{O}(N \log N \log M)$ and requiring $\mathcal{O}(N \log M)$ qubits for a system of N electrons and M orbitals. This way, plane-wave Hamiltonian simulations can be done efficiently in the first-quantization before converting to the second quantization to apply electron non-conserving operations. Similarly, second-quantized Hamiltonian simulation algorithms can take advantage of efficient measurement circuits originally designed for the first-quantized representation. We discuss applications of this hybrid quantization scheme to bring polynomial circuit improvements in the characterization of ground-state and excited-state properties, and in performing *ab-initio* molecular dynamics (AIMD) calculations.

Introduction

Performing chemical experiments *in-silico* has been the cornerstone of many scientific discoveries and commercial applications. Research in this direction spans a wide range of areas, including Hamiltonian dynamics, thermochemistry [1], computational spectroscopy [2–4], and electron transfer reactions [5–7]. Most simulations rely on solving eigenstates and applying the time evolution of the Hamiltonian. However, classical algorithms based on the many-body Hamiltonian often have a trade-off in accuracy and efficiency. The Full Configuration Interaction (FCI) [8] offers high accuracy but is computationally prohibitive, with a cost of $\mathcal{O}(M^{3N})$ for a system of M orbitals and N electrons, restricting its use to small systems. The Coupled Cluster method [9, 10], commonly with Single and Double excitations (CCSD), provides a practical approximation to FCI, reducing the complexity to $\mathcal{O}(M^3N^3)$. However, even this reduced cost remains impractical for large molecular systems or periodic solids with a large number of orbitals. Mean-field methods, such as Density Functional Theory (DFT), are widely adopted due to their low computational cost of $\mathcal{O}(N^3)$. However, they often lack the accuracy of more advanced methods and are not well-suited for studying excited states.

Recent advances in quantum computing technologies have sparked interest in developing quantum algorithms to tackle quantum chemistry challenges. A distinctive

feature of quantum computers is the ability for M qubits to represent a linear combination of 2^M states. This capability enables efficient encoding of both first- and second-quantized many-body wavefunctions. Using this superposition of qubits, quantum algorithms like Quantum Phase Estimation (QPE) [13, 20–24] can operate simultaneously on these states, potentially surpassing classical algorithms in scaling efficiency to solve equilibrium properties for chemical systems. For preparing the eigenstate, the most efficient algorithm for the plane-wave basis-set is done in the first quantization with a Toffoli complexity of $\mathcal{O}(N^{8/3}M^{1/3} + N^{4/3}M^{2/3})$ [13, 22]. In contrast, the second-quantized representation provides a more efficient algorithm for the molecular orbital (MO) basis, with a Toffoli complexity of $\mathcal{O}(M^2)$ [15]. Efficient algorithms for measuring chemical properties, such as the k -RDMs [14, 16, 17, 25–27], have also been developed for both quantizations. In the first quantization, all the k -RDMs can be estimated with $\mathcal{O}(k^k N^k \log M / \varepsilon^2)$ measurements using classical shadows [14], given a specified k and an allowable error of ε . In the second quantization, amplitude estimation [16] achieves the same with $\mathcal{O}(M^k / \varepsilon)$ measurements. For comparison, classical calculations of the 2-RDM costs $\mathcal{O}(N^2 M^2)$ for the FCI calculation [28] and $\mathcal{O}(N^4 M^4)$ for the CCSD calculation [29, 30].

Beyond solving equilibrium properties, the simulation of material and molecular non-equilibrium properties, such as dynamical correlations and AIMD, requires additional operations beyond eigenstate preparation and chemical properties measurements. Dynamical correlations like Green’s function calculations [4, 31–35] are crucial for studying the spectroscopic proper-

* kesson.yc.chen@foxconn.com

† alicehu@cityu.edu.hk

‡ min-hsiu.hsieh@foxconn.com

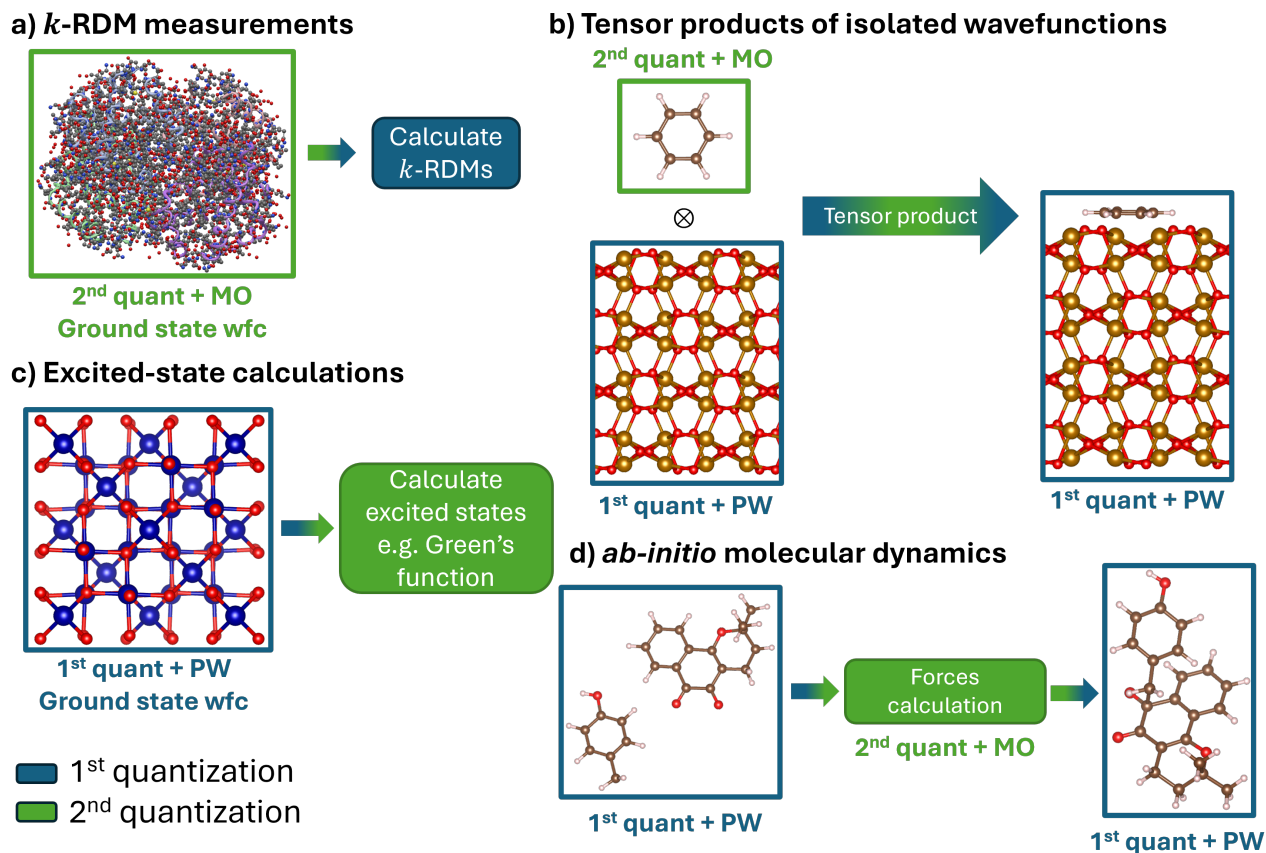


Figure 1. Illustrations of the applications of the hybrid quantization scheme. (a) The second-quantized ground-state wavefunction of a Haemoglobin complex is converted to the first-quantization for more efficient k -RDM measurements. (b) Hybrid quantization is used to perform tensor products of an isolated benzene molecule and an isolated Fe_2O_3 surface, eliminating the need to create empty vacuum space that is commonly used to isolate two disentangled systems. (c) The Green's function of a Co_3O_4 system was efficiently calculated switching to the first and second quantization. (d) Efficient AIMD simulations of the product β -lapachone [11] using the plane-wave basis for the ground-state preparation and the MO basis for the calculation of ionic forces.

ties [3], which can be experimentally validated using techniques such as photoemission spectroscopy [4, 34]. These calculations involve ground-state preparation, electron non-conserving operators, Hamiltonian inversion, and Hadamard tests. Similarly, AIMD simulations iterate through the electronic ground state preparation, ionic forces calculation, ionic simulation, and electronic Hamiltonian update steps, offering a first-principles approach to phenomena like hydrogen bonding, unlike classical semi-empirical methods [36, 37]. While VQE-based AIMD [38, 39] for noisy intermediate-scale quantum devices has been explored, fault-tolerant quantum-based AIMD, even with pseudo-ion approximation [40], allows researchers to explore larger and more complex systems, such as enzymatic reactions, nanoparticle formation [41], and atmospheric degradation of volatile organic compounds [42].

For these types of calculations, however, each step of the simulation workflow must be scrutinized for potential bottlenecks when selecting an appropriate quantiza-

tion. To tackle these inefficiencies, we propose conversion circuits that enable seamless transitions between quantization methods, shown in Theorem 1. This approach allows one to adopt the most efficient quantization for each simulation step, rather than adhering to a single method throughout the entire workflow. To increase the variety of potential applications for our hybrid quantization framework, we also introduced Corollary 1, which allows efficient transformations between the plane-wave and the MO basis in the first quantization.

We then showcase applications of both Theorem 1 and Corollary 1, which mostly show polynomial improvements over the previous solutions as shown in Table I. Our first application addresses ground-state materials characterization, where the hybrid quantization framework allows different quantization to be used for the ground-state preparation and k -RDM measurement steps. In this case, an improvement is found for the case of MO Hamiltonians with $N \ll M$, where we used the second-quantized ground-state preparation and first-

Table I. Summary of complexity differences between the first-quantized and second-quantized representations for various quantum simulation problems. The hybrid quantization framework that we proposed is shown underlined in the Table below, where we show potential workflow paths that result in better Toffoli complexities. “Electronic wavefunction characterization of materials” contains purely quantum simulation workflows concerning only the electronic degrees of freedom. Hence, only the quantum costs are included. Conversely, the “Dynamic Hamiltonian simulation” contains a hybrid simulation workflow, where the electrons are simulated using quantum computers and the ions are simulated using classical computers via the Born-Oppenheimer approximation [12]. The variable N represents the number of electrons while M represents the number of orbitals, with M_{MO} and M_{PW} indicating that the cost scaling is specifically for the MO and plane-wave basis, respectively ($M_{MO} \ll M_{PW}$). Similarly, ε_{QPE} , ε_{RDM} , and ε_{HAD} are error parameters for the QPE simulations, RDM measurements, and Hadamard tests, respectively. For the row “Ground-state characterization (whole molecular system)”, we estimate the cost of measuring all the k -RDMs. On the other hand, the row “Ground-state characterization (defect/adsorbed periodic system)” shows the cost of measuring a small subset of \mathcal{M} observables localised near the defect or adsorbed complex.

Electronic wavefunction characterization of materials		
	Hamiltonian simulation	Measurement
Ground-state characterization (whole molecular system)	1st quant: $\mathcal{O}(N^{4/3}M_{PW}^{2/3}/\varepsilon_{QPE})$ [13]	$\mathcal{O}(k^k N^k \log M_{PW}/\varepsilon_{RDM})$ [14] ($N \ll M_{PW}$)
	2nd quant: $\mathcal{O}(M_{MO}^{2.1}/\varepsilon_{QPE})$ [15]	$\mathcal{O}(M_{MO}^k/\varepsilon_{RDM})$ [16, 17] ($N \approx M_{MO}$)
	Hybrid: $\mathcal{O}(M_{MO}^{2.1}/\varepsilon_{QPE})$ [15]	$\mathcal{O}(N \log N \log M_{MO} + k^k N^k \log M_{MO}/\varepsilon_{RDM})$ [14] ($N \ll M_{MO}$)
Ground-state characterization (defect/adsorbed periodic system)	1st quant: $\mathcal{O}(N^{4/3}M_{PW}^{2/3}/\varepsilon_{QPE})$ [13]	$\mathcal{O}(k^k N^k \log M_{PW}/\varepsilon_{RDM})$ [14]
	2nd quant: $\mathcal{O}(M_{MO}^{2.1}/\varepsilon_{QPE})$ [15]	$\mathcal{O}(\sqrt{\mathcal{M}}/\varepsilon_{RDM})$ [16, 17]
	Hybrid: $\mathcal{O}(N^{4/3}M_{PW}^{2/3}/\varepsilon_{QPE})$ [13]	$\mathcal{O}(NM_{PW} + \sqrt{\mathcal{M}}/\varepsilon_{RDM})$ [16, 17] (PW \rightarrow MO)
Excited-state characterization (Eqn. 3)	1st quant: Not applicable	Not applicable
	2nd quant: $\mathcal{O}(M_{PW}^{7/3})$	$\mathcal{O}(1/\varepsilon_{HAD}^2)$ [18] (PW dual basis [19])
	Hybrid: $\mathcal{O}(NM_{PW}^{2/3})$	$\mathcal{O}(1/\varepsilon_{HAD}^2)$ [18]
Dynamic Hamiltonian simulation		
	Classical cost	Quantum cost
Born-Oppenheimer [12] AIMD simulation	1st quant: $\mathcal{O}(M_{PW}^4)$	$\mathcal{O}(N^{4/3}M_{PW}^{2/3}/\varepsilon_{QPE} + N^2 \log M_{PW}/\varepsilon_{RDM}^2)$
	2nd quant: $\mathcal{O}(M_{MO}^6)$	$\mathcal{O}(M_{MO}^{2.1}/\varepsilon_{QPE} + M_{MO}^2/\varepsilon_{RDM})$
	Hybrid: $\mathcal{O}(M_{MO}^4)$	$\mathcal{O}(N^{4/3}M_{PW}^{2/3}/\varepsilon_{QPE} + NM_{MO}M_{PW} + M_{MO}^2/\varepsilon_{RDM})$

quantized k -RDM measurements, as illustrated in Figure 1(a). The opposite conversion can also be useful in other situations, such as when we are only concerned about characterizing a defect or adsorption site, in which measuring a smaller number of localized observables is sufficient for the study. In this case, the ground-state is prepared in the first quantization using the plane-wave basis, transformed to the MO basis using Corollary 1, and converted to the second-quantization. We also explored the preparation of initial states of an adsorbed system under many different atomic configurations by applying a tensor product implemented using the hybrid quantization framework as shown in Figure 1(b).

The next application is the characterization of materials in the excited state, where polynomial improvement in gate complexity is realized during the calculation of the Green’s function using the plane-wave basis-set (Figure 1(c)). The computation contains parts that are efficient in the first quantization, notably in calculating the reciprocal of the Hamiltonian, and parts which cannot be performed in the first quantization, such as applying the electron non-conserving fermionic creation and annihilation operators. As a result, we are forced to use the less efficient second-quantized algorithm to calculate

the Green’s function. Our hybrid approach leverages the efficiency of the first-quantized Hamiltonian reciprocal algorithm and then converts to the second quantization for the electron non-conserving operations, leading to significant gate complexity improvements.

Finally, we showcase the use of our hybrid framework in improving the classical costs associated with AIMD simulations, depicted in Figure 1(d). AIMD simulations in the MO basis incurs large classical costs when updating the Hamiltonian to the new atomic positions, while the simulation in the plane-wave basis incurs large classical cost when calculating the forces acting on the ions. Using Corollary 1, we propose preparing the ground state in the plane-wave basis, converting to the MO basis for efficient ionic force calculation, and then reverting back to the plane-wave basis to circumvent the costly Hamiltonian updates inherent in the MO basis.

Results

Hybrid Quantization Framework

The many-body wavefunction of fermionic systems can be expressed in the first or the second quantization, both serving distinct purposes. The first quantization straightforwardly expresses the many-body wavefunction as a tensor product of the respective single-particle wavefunc-

tion. It only expresses wavefunctions with the same number of particles, simplifying the construction of operators. This led to efficient Hamiltonian simulations for certain bases, such as plane waves. Conversely, the second quantization aims for an antisymmetrized basis for the many-body wavefunction, necessitating the Slater determinant, which tracks the occupation of each orbital. This allows the second quantization to excel in scenarios where particle number fluctuates. The handling of the Pauli exclusion principle also differs between the two. The first quantization requires the wavefunction to be antisymmetrized, while the second quantization delegates that responsibility to the operators, which complicates second-quantized operator implementations. To apply these settings, different fermion-to-qubit encodings [43–53] are proposed.

For accurate calculations of the electronic structure, orbitals are required to vastly outnumber electrons as $N \ll M$. The optimal encoding, where both qubit and gate complexity are logarithmically dependent on M , can be realized using variants of the binary addressing code [50] for both the first [13, 22] and second [53] quantizations. The first optimal variant is the “first-quantized encoding”, used for first-quantized Hamiltonian simulations that are specified in the plane-wave basis [13, 22, 54]. It uses N registers, each comprising $\mathcal{O}(\log M)$ qubits, to store the binary representation of the orbital indices, resulting in a qubit scaling of $\mathcal{O}(N \log M)$. State-of-the-art techniques in the first quantization also leverage this code with $\mathcal{O}(\log M)$ gate operations (e.g., binary arithmetic and comparison) per register, totalling a gate cost of $\mathcal{O}(N \log M)$. A unique advantage of the first quantization is its efficiency in the plane-wave basis, enabling large material simulations. Another optimal variant is the “sorted-list encoding” [53], used for second-quantized Hamiltonian simulations with Majorana operators. This mitigates the inefficiency of the binary addressing code, where the decomposition of fermionic operators to Pauli operators is prohibitively expensive due to its non-linear nature [50]. An ascending-order constraint ensures Slater determinants remain order-independent, and fermionic operators now match the $\mathcal{O}(N \log M)$ gate cost of first quantization. A unique advantage of the second quantization is the encoding of “unoccupied” orbitals, enabling representation of Slater determinants with different electron numbers and supporting electron non-conserving operators. Further details on both quantizations can be found in Section A.1 of the Supplementary Information (SI).

The two encodings described above serves different purposes in the two quantizations, but the similar binary addressing encoding bridges the two quantization. This insight enables efficient conversion between the two quantizations realized via Theorem 1, allowing a hybrid approach that switches between quantizations mid-simulation to exploit the strengths of each quantizations while avoiding their limitations, showcasing a drastic improvement on resource requirement in material and

molecular simulation.

Theorem 1. *Conversion between the first-quantized encoding and the sorted-list encoding can be performed with a gate cost of $\mathcal{O}(N \log N \log M)$ with a qubit complexity of $\mathcal{O}(N \log M)$.*

Proof. The proof can be found in the Methods section. \square

In order to leverage the hybrid quantization framework to its full potential, we also introduced basis transformation in the first quantization. Consider a single-particle basis transformation matrix U of dimension $M_1 \times M_2$. The application of this basis transformation matrix facilitates the conversion between different bases, such as from the MO basis to the plane-wave basis. This transformation can be expressed in first and second quantization as

$$\psi_i^{(1)} = \sum_j U_{ij} \psi_j^{(2)} \quad \text{and} \quad (a_i^{(1)})^\dagger = \sum_j U_{ij} (a_j^{(2)})^\dagger,$$

respectively. The second quantization has efficient circuits when $M_1 = M_2 = M$. In that case, we would first express the global transformation matrix \mathbb{U} for the Slater determinant as

$$\mathbb{U} = \exp \left(\sum_{ij} [\log U_{ij}] (a_i^\dagger a_j - a_j^\dagger a_i) \right).$$

This can be decomposed into $\binom{M}{2}$ Pauli rotations, resulting in a total gate complexity of $\mathcal{O}(M^2)$ for the Jordan-Wigner encoding, and $\mathcal{O}(M^2 N \log M)$ for the sorted-list encoding. When $M_1 \neq M_2$, the basis transformation matrix U must be extended to a unitary of dimension $\max(M_1, M_2) \times \max(M_1, M_2)$, resulting in a total gate complexity of $\mathcal{O}(\max(M_1, M_2)^2)$. On the other hand, basis transformations in the first quantization is detailed in Corollary 1.

Corollary 1. *Basis transformations in the first-quantized encoding can be performed by applying the single-particle basis transformation matrix once for each of the N registers. Those registers contains $\lceil \log_2 M \rceil$ qubits each, which stores the binary representation of the orbital index occupied by each of the N electronic degrees of freedom. As a result, implementing a $M_1 \times M_2$ basis transformation matrix would, in the worst-case, involve single-qubit gates and $\mathcal{O}(NM_1 M_2)$ CNOT gates [55].*

Proof. The proof can be found in the Methods section. \square

While the complexity in Corollary 1 represents a worse-case scenario, practical implementations are often less costly. For example, converting between the plane-wave and plane-wave dual basis in second quantization uses the Fermionic Fast Fourier Transform (FFFT) circuit [56], achieving a gate cost of $\mathcal{O}(M^2)$. In first quantization,

the same transformation leverages the Quantum Fourier Transform (QFT) [57, 58] applied to each of the N registers spanning $\mathcal{O}(\log M)$ qubits, resulting in a gate cost of $\mathcal{O}(N \log M \log \log M)$.

Applications

In this section, we explore the hybrid quantization framework, an innovative approach that merges the strengths of first and second quantization to tackle complex quantum problems with greater efficiency and flexibility. This framework is particularly useful when traditional methods fall short, offering a powerful tool for advanced simulations. We will dive into three key scenarios where it proves invaluable: ground-state materials characterization, excited state materials characterization, and Born-Oppenheimer AIMD simulation. A cartoon depiction of these applications is illustrated in Figure 1.

Ground-state characterization. Characterization of materials using quantum computers involves two major steps: Hamiltonian simulation to prepare the ground state, and the measurement of observables with respect to the ground state. Examples of such observables are ionic forces used in molecular dynamics simulation, and the Hessian matrix of the Hamiltonian used in obtaining vibrational frequencies for computational thermochemistry. As such observables are typically expressed in terms of the second-quantized creation and annihilation operators, their expectation values can be calculated by measuring the reduced density matrices (RDMs) of the ground state wavefunctions

$$O = \sum_{pq} o_{pq} a_p^\dagger a_q \implies \langle \hat{O} \rangle = \sum_{pq} o_{pq} \langle a_p^\dagger a_q \rangle.$$

While the observable above only contains one-electron terms, this can be generalized to the expectation value of k -electron terms called k -RDMs

$${}^k D_{q_1, \dots, q_k}^{p_1, \dots, p_k} = \langle a_{p_1}^\dagger \dots a_{p_k}^\dagger a_{q_k} \dots a_{q_1} \rangle.$$

Many algorithms have been developed to estimate the k -RDMs, including sampling [59–61], amplitude estimation [16, 27, 62], shadow tomography [63, 64], and classical shadows [14, 17, 25]. In general, when N is not much smaller than M , amplitude estimation is optimal with $\mathcal{O}(M^k/\epsilon)$ measurements and $\mathcal{O}(M^k/\epsilon)$ fermionic evolution gates.

However, in the $N \ll M$ regime, k -RDM measurements are more efficient using classical shadow in the first quantization. It can measure the set of all k -RDMs up to an error of ϵ by measuring $\mathcal{O}(k^k N^k \log M/\epsilon^2)$ circuits [14], each comprising $\mathcal{O}(N \log^2 M)$ Clifford gates, which outperforming second quantized classical shadow algorithms that utilise particle-conserving symmetry [26]. For Hamiltonian simulations performed in the second quantization, conversion to the first-quantized encoding enables more efficient measurements via classical shadows, as shown in Figure 2(a). With a conversion circuit, the second-quantized sorted-list encoding combined with

the first-quantized classical shadow can have a logarithmic dependence on the orbital number M for all qubit, gate, and measurement complexities, as shown in the first row of Table I.

But this does not imply that every calculation in the $N \ll M$ regime should employ the first-quantized classical shadow algorithm. The second-quantized amplitude estimation algorithm [16] exhibits better scaling with respect to ϵ and allows an arbitrary set of observables, where \mathcal{M} observables can be measured with $\mathcal{O}(\sqrt{\mathcal{M}}/\epsilon)$ measurements and $\mathcal{O}(\sqrt{\mathcal{M}}/\epsilon)$ gates. This approach proves beneficial when investigating defects or surface adsorption in periodic systems, where the focus is primarily on obtaining observables localised to the defect or adsorption site, rather than the bulk properties of the system. If we utilise a more localised basis of size \mathcal{M} to describe the defect or adsorption region, we have $\mathcal{M} \ll N \ll M$. The basis could either be the real-space basis derived from the Fourier transform of the plane-wave basis, or the even smaller MO basis. Consequently, we would prepare the ground state using the plane-wave basis in the first-quantization, apply basis transformation to the smaller basis localised around the defect or adsorption region (via Corollary 1), and switch to the second quantization for the amplitude estimation algorithm [16]. The advantage of this technique is demonstrated in the second row of Table I.

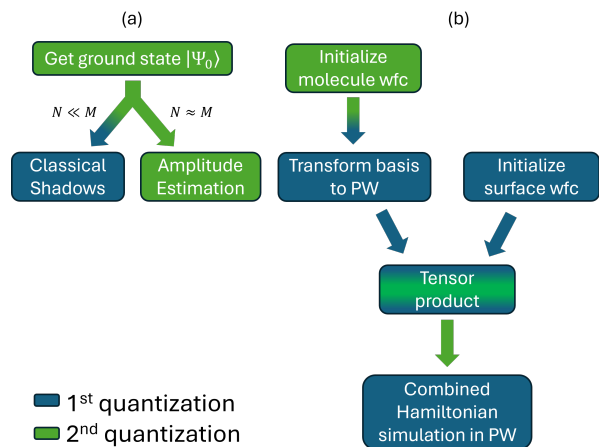


Figure 2. Workflow to (a) measure reduced density matrices (b) perform a tensor product between the wavefunction of a molecule in the MO basis and the wavefunction of a surface in the plane-wave basis.

Aside from increasing the efficiency of observable measurements, the hybrid quantization framework could also be utilized to improve the ground-state preparation step in certain situations. Consider the time-evolution calculation of a molecule as it is adsorbed onto a surface. We initialise the system with the unentangled ground state of the molecule and the ground state of the surface. Conventionally, we would place the molecule and

the surface in the same simulation cell with a large vacuum space between the two to ensure no entanglement. The ground state is then obtained in the first quantization using the plane-wave basis set. However, the long-range nature of the Coulomb term would require a very large vacuum space, significantly increasing the number of plane waves. As a rough example, DFT calculations of the Fe_2O_3 (01 $\bar{1}2$) surface with an unentangled benzene molecule, as shown in Figure 1(b), require approximately $\sim 6.5 \times 10^5$ more plane waves compared to the surface alone (Figure 3). As detailed in Section A.2 of the SI, actual computational savings likely exceed this estimate as the plane wave cutoffs for many-body quantum simulation are much higher.

This inefficiency can be avoided by computing the ground states of the molecule and surface as isolated systems, followed by their tensor product. The molecule’s ground state may even be calculated in the MO basis, which requires transformation to the plane-wave basis (per Corollary 1) to align with the surface’s plane-wave basis before applying the tensor product. The resulting wavefunction is then evolved under the Hamiltonian of the combined system.

Applying the tensor product naively in the sorted-list encoding violates its ascending-order requirement and may introduce states with duplicate orbital indices, necessitating their removal from the wavefunction. Similarly, in the first quantization, the tensor product breaks the antisymmetric property. As a result, this tensor product represents a novel application of the hybrid quantization scheme, as both the first and second quantization face significant limitations in their implementation. Unlike the other applications, where the suboptimal quantization may suffice, this application requires the conversion circuit. To address these challenges, we would first perform the tensor product in the second-quantized sorted-list encoding by concatenating the qubit representation of the two systems. A sorting network then restores the ascending-order requirement, with Z gates applied for each swap to account for the parity. The wavefunction is subsequently converted to the first quantization, with the states containing duplicate orbital indices flagged by an ancilla qubit using $\mathcal{O}(N)$ comparisons, yielding the tensor product in the first quantization.

Another application involves identifying active sites in enzymes or catalysts, where we need to perform multiple ground-state calculations of the reactant-catalyst systems across various atomic configurations. Without the hybrid quantization framework, those ground-state calculations of multiple different atomic configurations are independent calculations. Thus, given N_{search} atomic configurations to calculate, we would incur a cost of $\mathcal{O}(N_{\text{search}}\lambda/\alpha)$ [65, 66] qubitization circuits, with α being the overlap between the initial state and the ground state. With the hybrid quantization framework, the ground states of the catalyst and the reactants are first prepared independently and their tensor product are used as effec-

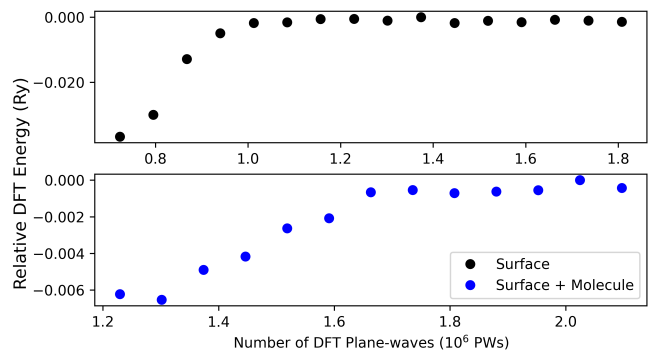


Figure 3. The DFT energies of the Fe_2O_3 (01 $\bar{1}2$) surface (top) and the same surface with a benzene molecule (bottom) for different simulation cell heights. The simulation details can be found in Section A.2 of the SI.

tive initial states for the ground-state simulation of the combined system, greatly increasing the α of the previous cost scaling. For enzymes or zero-dimensional catalysts, both components are represented in the MO basis. For two-dimensional catalysts, the reactant remains in the MO basis, while the catalyst is described using the plane-wave basis, as illustrated in Figure 2(b). To proceed, both ground states are transformed to the basis of the combined system using Corollary 1, followed by the application of the tensor product. Here, we would use the procedure outlined in the previous example to perform the tensor product.

Excited-state characterization. For this example, we focus on the study of low-lying excited state properties, namely the ionization and electron attachment processes of periodic systems with the plane-wave basis-set. The plane-wave basis-set favours the first-quantized Hamiltonian simulation algorithm for efficient computation. However, those processes are electron non-conserving which necessitates the second-quantized representation. An example of this is the ionization and electron attachment probabilities [35], written as

$$\begin{aligned} \lambda_{h,i,n} &= |\langle \Psi_{N_0-1,n} | a_i | \Psi_{N_0,0} \rangle|^2 \text{ and} \\ \lambda_{p,i,n} &= |\langle \Psi_{N_0+1,n} | a_i^\dagger | \Psi_{N_0,0} \rangle|^2, \end{aligned} \quad (1)$$

respectively. In this case, N_0 denotes the electron count for a neutral systems, $|\Psi_{N,n}\rangle$ is the n -th excited state of the N -electron system, with $n = 0$ being the ground state. To calculate the above probabilities, we are forced to use the suboptimal second-quantized plane-wave Hamiltonian simulation algorithm as a_i and a_i^\dagger are electron non-conserving. With the hybrid quantization framework, we could prepare $|\Psi_{N_0,0}\rangle$ and $|\Psi_{N_0\mp 1,n}\rangle$ in the first quantization and apply a_i or a_i^\dagger in the second quantization. The Hadamard test workflow, depicted in Figure 4(a), would then involve the preparation of $|\Psi_{N_0,0}\rangle$, conversion to second quantization, application of a_i or a_i^\dagger , conversion back to first quantization, and finally the conjugate preparation of $|\Psi_{N_0\mp 1,n}\rangle$. Since the

conversion circuit costs $\mathcal{O}(N \log N \log M)$ gates and the application of a_i or a_i^\dagger in the sorted-list encoding costs $\mathcal{O}(N \log M)$ gates, the complexity of this whole procedure is dominated by the preparation of $|\Psi_{N_0,0}\rangle$ and $|\Psi_{N_0\mp 1,n}\rangle$. The ground-state preparations costs $\mathcal{O}(\lambda/\alpha)$ queries to the qubitization circuits, where α is the overlap between the target ground state and the initial guess wavefunction [65, 66]. Thus, the Toffoli scaling advantage of the hybrid quantization here is equal to the Toffoli scaling advantage of the first-quantized plane-wave Hamiltonian simulation.

Another example is the calculation of the Green's function, essential in calculating the optical properties of materials, performing computational spectroscopy, and studying electron transport and scattering [67, 68]. In fact, the ionization and electron attachment probabilities above contributes to the Green's function in the Lehmann representation [35], where δ below is an infinitesimally small positive number

$$G_\alpha(\omega) = \sum_{n=0}^M \frac{\lambda_{h,\alpha,n}}{\omega + i\delta - (E_0 - E_{N_0-1,n})} + \sum_{n=0}^M \frac{\lambda_{p,\alpha,n}}{\omega + i\delta - (E_{N_0+1,n} - E_0)}. \quad (2)$$

Another representation of the Green's function discussed in the literature [32], which only require the preparation of the ground state, is the following:

$$G_{ij}^{(+)}(z) = \langle \Psi_{N_0,0} | a_i (z - [H - E_0])^{-1} a_j^\dagger | \Psi_{N_0,0} \rangle, \quad (3)$$

$$G_{ij}^{(-)}(z) = \langle \Psi_{N_0,0} | a_j^\dagger (z + [H - E_0])^{-1} a_i | \Psi_{N_0,0} \rangle.$$

Similarly with the ionization and electron attachment probabilities, we would use the first quantization for optimal calculations of both the ground state $|\Psi_0\rangle$ and the application of the $(z \pm [H - E_0])^{-1}$ term, while performing the electron non-conserving a_i and a_j^\dagger parts in the second-quantized representation, with the workflow shown in Figure 4(b). In this case, the complexity of this procedure is dominated by the application of the $(z \pm [H - E_0])^{-1}$ term.

Using the preconditioned fast inversion algorithm [32], we can obtain a block-encoding of $(z \pm [H - E_0])^{-1}$ for some $\eta \geq |z|$ using $\mathcal{O}(N^6 M \ln(\delta^{-1})/\Omega \eta^2 \varepsilon)$ applications of the first-quantized qubitization algorithm (details in Section A.3 of the SI), offering a significant improvement in the plane-wave basis where $N \ll M$. For comparison, the second-quantized Jordan-Wigner encoding using the plane-wave dual basis scales as $\mathcal{O}(M^5 \ln(\delta^{-1})/\Omega^2 \eta^2 \varepsilon)$ [32]. Alternatively, we could also use the non-preconditioned inversion method [19]. In this case, the block-encoding of $(z \pm [H - E_0])^{-1}$ is achieved using $\mathcal{O}(NM^{2/3}/\Omega^{2/3} \eta^2 \varepsilon + N^2 M^{1/3}/\Omega^{1/3} \eta^2 \varepsilon)$ applications of the first-quantized Hamiltonian (details in Section A.3 of the SI), compared to $\mathcal{O}(M^{7/3}/\Omega^{2/3} \eta^2 \varepsilon)$ applications for the second-quantized Jordan-Wigner encoding [32], as summarized in the third row of Table I.

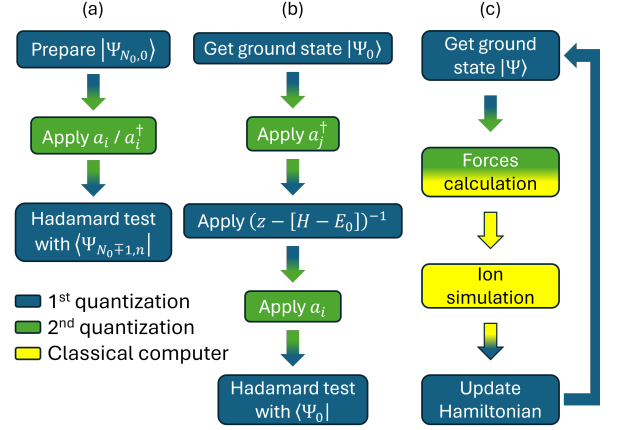


Figure 4. Workflow to (a) measurement of ionization and electron attachment probabilities of Equation 1, (b) measurement of the Green's function of Equation 3, and (c) perform BO-AIMD simulations in the plane-wave basis while using the MO basis to extract RDMs for the calculation of atomic forces.

Born-Oppenheimer AIMD simulation. This example focuses on Born-Oppenheimer AIMD (BO-AIMD) [12] simulations using both the MO and plane-wave bases. Due to the Born-Oppenheimer approximation, the electronic degrees of freedom are simulated in quantum computers, while the nuclear degrees of freedom are simulated in classical computers. As a result, a typical BO-AIMD simulation workflow comprises four iterative steps: electronic ground-state preparation, electronic forces calculations, ion simulation, and finally updating the electronic Hamiltonian, with the costs summarized by the four rows of Table II. These steps are repeated for a predetermined number of time steps.

First, the ground-state is prepared using $\mathcal{O}(\lambda/a)$ applications of the qubitization circuits [65, 66], where $a = \langle \Psi_{\text{init}} | \Psi_g \rangle$ is the overlap between the initial state and the ground state. Next, forces exerted by the electrons acting on the ions are calculated. Using Hellmann-Feynman theorem [38, 69], the forces can be written as the ground-state expectation values of the Hamiltonian's first derivative with respect to the ionic positions \mathbf{R}_I as:

$$\mathbf{F} = - \left\langle \Psi \left| \frac{dH}{d\mathbf{R}_I} \right| \Psi \right\rangle = - \sum_{pq} \frac{dh_{pq}}{d\mathbf{R}_I} \langle \Psi | a_p^\dagger a_q | \Psi \rangle - \sum_{pqrs} \frac{dh_{pqrs}}{d\mathbf{R}_I} \langle \Psi | a_p^\dagger a_q^\dagger a_r a_s | \Psi \rangle.$$

This requires measurement of the 1- and 2-RDMs along with a classical computations with costs of $\mathcal{O}(N_{\text{ion}} M_{MO}^4)$ for the MO basis and $\mathcal{O}(N_{\text{ion}} M_{PW}^3)$ for the plane-wave basis, where N_{ion} represents the number of ions. The slight reduction for the plane-wave basis comes from the conservation of momentum reducing the number of two-electron terms. The third step is the simulation of the

Table II. Summary of the complexity differences of Born-Oppenheimer AIMD between the MO and the plane-wave basis ($M_{MO} \ll M_{PW}$) along with a hybrid basis scheme that only uses the MO basis during RDM measurements. For the row “Electronic ground-state preparation”, $a = \langle \Psi_{\text{init}} | \Psi_g \rangle$ represents the overlap between the initial state and the ground state [65, 66]. N_{ion} represents the number of ions in the simulation. The steps below are repeated until the predetermined number of time steps is reached, and the underline is the main additional cost in the first and second quantization.

Workflow steps	MO basis	PW basis	Hybrid basis
Electronic ground-state preparation	Quantum cost: $\mathcal{O}(M_{MO}^{2.1}/a)$ [15] (2 nd quant)	$\mathcal{O}(N^{8/3}M_{PW}^{1/3}/a + N^{4/3}M_{PW}^{2/3}/a)$ (1 st quant)	
Electronic forces calculation	Quantum cost: $\mathcal{O}(M_{MO}^2/\varepsilon_{\text{RDM}})$ [16, 17]	$\mathcal{O}(N^2 \log M_{PW}/\varepsilon_{\text{RDM}}^2)$ [14]	$\mathcal{O}(NM_{MO}M_{PW})$ PW \rightarrow MO $\mathcal{O}(N \log N \log M_{MO})$ 1 st \rightarrow 2 nd $\mathcal{O}(M_{MO}^2/\varepsilon_{\text{RDM}})$ [16, 17] RDMs
	Classical cost: $\mathcal{O}(N_{\text{ion}}M_{MO}^4)$	$\mathcal{O}(N_{\text{ion}}M_{PW}^3)$	$\mathcal{O}(N_{\text{ion}}M_{MO}^4)$
Ion simulation	Classical costs: $\mathcal{O}(N_{\text{ion}}^2)$	$\mathcal{O}(N_{\text{ion}}^2)$	$\mathcal{O}(N_{\text{ion}}^2)$
Update electronic Hamiltonian	Classical cost: $\mathcal{O}(M_{MO}^6)$	Negligible [13]	Negligible [13]
	Quantum cost: $\mathcal{O}(M_{MO}^2)$	Not applicable	Not applicable

ions, where the forces obtained from the previous step is used to move the ions using classical mechanics, which should scale by $\mathcal{O}(N_{\text{ion}}^2)$.

Finally, the electronic Hamiltonian is updated to reflect the new positions of the ions. For BO-AIMD calculations with the MO basis, additional complexity arises in this step from the dependence of basis functions on atomic positions as shown in the fourth row of Table II. First, the h_{pq} and h_{pqrs} integrals must be recalculated at every time step, with classical costs of $\mathcal{O}(M^6)$ incurred when constructing efficient qubitization circuits using rank-reduction techniques, such as single-factorization [70], double-factorization [71], and tensor hypercontraction [15]. Additionally, reusing the previous ground-state wavefunction as the initial guess for the updated Hamiltonian requires transforming the previous wavefunction to the basis of the updated MO orbitals. This incurs a classical cost of $\mathcal{O}(M_{MO}^2)$ for calculating the basis transformation matrix and a quantum gate cost of $\mathcal{O}(M_{MO}^2)$ for implementing the basis transformation in a quantum circuit. On the other hand, plane-wave BO-AIMD simulations require only minor modifications to the qubitization circuits [13] for ground state preparation, as the plane-wave basis functions do not depend on atomic positions. Similarly, the previous ground-state wavefunction of a plane-wave simulation can also be immediately reused as the initial guess for the updated Hamiltonian without any basis transformation step.

Nevertheless, the calculation of atomic forces still incurs a significant $\mathcal{O}(N_{\text{ion}}M_{PW}^3)$ classical cost, particularly when considering the orders of magnitude greater number of plane-waves required compared to MOs to achieve similar levels of precision. Hence, BO-AIMD us-

ing the MO basis in second quantization may still provide efficiency advantages compared to the plane-wave basis. To circumvent the expensive classical cost incurred when calculating the atomic forces, BO-AIMD calculations in the plane-wave basis can be transformed to the MO basis in second quantization during the RDM measurements, with the workflow shown in Figure 4(c). This reduces the classical cost during the calculation of atomic forces to $\mathcal{O}(N_{\text{ion}}M_{MO}^4)$, where $M_{MO} \ll M_{PW}$, and allows us to utilise the better error scaling of the second-quantized amplitude estimation algorithm [16] as shown in the “Hybrid basis” column of Table II. To achieve this, Corollary 1 is used to convert the plane-wave basis to the MO basis, before converting the system to the second quantization via Theorem 1. The scaling advantages for this hybrid basis scheme is illustrated in the last column of Table II. While the conversion from the plane-wave to MO bases is expected to incur some errors, we do not expect such errors to be significant, especially when using large plane-wave cutoffs. Alternatively, a specifically designed localised basis, that minimises these errors, could be used instead of an off the shelf MO basis.

Discussion

In this study, we present a hybrid quantization scheme that significantly enhances material simulations by enabling efficient transitions between first- and second-quantized encodings. This approach achieves polynomial improvements through an efficient $\mathcal{O}(N \log N \log M)$ conversion circuit, optimising the Toffoli complexity for each simulation step. This scheme also mitigates limitations inherent to both encodings, such as applying particle non-conserved operators in the first quantization, while preserving the optimal efficiency of plane-wave and

MO Hamiltonian simulations. Additionally, the hybrid quantization scheme facilitates the combination of quantum states prepared in distinct bases, addressing challenges in tensor product operations of isolated wavefunctions. We also introduced a basis transformation algorithm for the first-quantized encoding, allowing quantum simulations to efficiently switch between the plane-wave and MO bases.

Prior work has utilized the antisymmetrization circuit [72] to convert the Jordan-Wigner encoding to the first-quantized encoding for efficient k -RDM measurements [14]. Our hybrid quantization scheme improves on this by introducing the reverse conversion. Furthermore, the sorted-list encoding [53] is used instead for the second-quantized counterpart, greatly simplifying the conversion and reducing the qubit requirement of both quantizations to $\mathcal{O}(N \log M)$. This, in turn, also opens up the sorted-list encoding to additional applications, especially in encoding electron non-conserving operations that is applied to first-quantized wavefunctions.

As our hybrid quantization framework uses the sorted-list encoding for the second-quantized representation, future research should focus on implementing and benchmarking this encoding in various Hamiltonian simulation algorithms, such as trotterization and qubitization. While our conversion circuit converts between the first-quantized encoding and the sorted-list encoding, the principles extend to other potential conversion circuits. Hence, exploring alternative circuits for different first- and second-quantized encodings remain a compelling avenue for further investigation.

Methods

Proof of Theorem 1. The conversion from the sorted-list encoding to the first-quantized encoding can be performed using the antisymmetrization circuit [72]. In total, they reported a gate cost of $\mathcal{O}(N \log N \log M)$ and an ancilla cost of $\mathcal{O}(N \log N)$. The gate cost here is dominated by the implementation of a reverse sorting network which applies a Z gate when any two registers are swapped.

On the other hand, the conversion from the first-quantized encoding to the sorted-list encoding is simpler. Given an antisymmetrized first-quantized state, we would simply sort the states in an ascending order through the use of a sorting network shown in the following equation

$$\sum_{\sigma \in S_N} \text{sgn}(\sigma) |i_{\sigma(1)}\rangle \otimes |i_{\sigma(2)}\rangle \otimes \cdots \otimes |i_{\sigma(N)}\rangle \xrightarrow{\text{sort}} |i_1\rangle \otimes |i_2\rangle \otimes \cdots \otimes |i_N\rangle \quad (i_1 < i_2 < \cdots < i_N).$$

Here, the left hand side represents the first-quantized representation of a Slater determinant with S_N representing the symmetric group of N symbols, and $\text{sgn}(\sigma)$ denotes the sign of the permutation. Similarly with the antisymmetrization circuit, a Z gate is also applied when any two registers are swapped to account for the $\text{sgn}(\sigma)$ term. The sorted-list state shown on the right-hand side above is obtained after the registers are sorted. As a result, the conversion from the first-quantized encoding to the sorted-list encoding also costs $\mathcal{O}(N \log N \log M)$ gates and $\mathcal{O}(N \log N)$ ancillae. \square

Proof of Corollary 1. Basis transformations of the single-particle wavefunctions can be represented with an $M_1 \times M_2$ matrix

$$\psi_i^{(1)}(\mathbf{x}) = \sum_j U_{ij} \psi_j^{(2)}(\mathbf{x}). \quad (4)$$

Thus, the basis transformation of a Hartree product can be performed by applying the matrix U to each electronic degrees of freedom

$$\Psi = \left(\sum_{j_1} U_{i_1 j_1} \psi_{j_1}^{(2)}(\mathbf{x}_1) \right) \otimes \cdots \otimes \left(\sum_{j_N} U_{i_N j_N} \psi_{j_N}^{(2)}(\mathbf{x}_N) \right).$$

In a quantum circuit, this basis transformation involves the circuit implementing U , applied to each of the N registers independently

$$|i_1\rangle \otimes \cdots \otimes |i_N\rangle \xrightarrow{U} (U|i_1\rangle) \otimes \cdots \otimes (U|i_N\rangle).$$

Assuming the worst-case complexity of an arbitrary dense matrix, U could be implemented using single-qubit gates and $\mathcal{O}(M_1 M_2)$ CNOT gates [55, 73]. With N electrons, the total complexity is $\mathcal{O}(N M_1 M_2)$. \square

ACKNOWLEDGEMENTS

A.H. gratefully acknowledges the sponsorship from City University of Hong Kong (Project No. 7005615, 7006103), CityU Seed Fund in Microelectronics (Project No. 9229135), and Hon Hai Research Institute (Project No. 9231594). This work was carried out using the computational facilities, CityU Burgundy, managed and provided by the Computing Services Centre at City University of Hong Kong (<https://www.cityu.edu.hk>).

AUTHOR CONTRIBUTIONS

The project was conceived by C.K. and Y.C. Theoretical results were proved by C.K. in discussion with M.H. Numerical simulations and analysis were performed by C.K. in discussion with A.H. All authors contributed to the write-up.

COMPETING INTERESTS

The authors declare no competing interests.

- [1] C. J. Cramer, *Essentials of Computational Chemistry: Theories and Models*, 2nd ed. (Wiley, Chichester, 2014).
- [2] J. J. Kas, J. J. Rehr, and F. D. Vila, in *International Tables for Crystallography* (John Wiley & Sons, 2022) pp. 107–113.
- [3] L. Nanni, *Computational and Theoretical Chemistry* **1227**, 114245 (2023).
- [4] S. Fomichev, P. A. M. Casares, J. Soni, U. Azad, A. Kunitsa, A.-C. Voigt, J. E. Mueller, and J. M. Arrazola, Fast simulations of X-ray absorption spectroscopy for battery materials on a quantum computer (2025), arXiv:2506.15784 [quant-ph].
- [5] Q. Wu and T. Van Voorhis, *Journal of Chemical Theory and Computation* **2**, 765 (2006).
- [6] Q. Wu and T. Van Voorhis, *The Journal of Chemical Physics* **125**, 164105 (2006).
- [7] B. Kaduk, T. Kowalczyk, and T. Van Voorhis, *Chemical Reviews* **112**, 321 (2012).
- [8] A. Szabo and N. S. Ostlund, *Modern Quantum Chemistry: Introduction to Advanced Electronic Structure Theory* (Dover Publications, Inc, Mineola, New York, 2012).
- [9] T. D. Crawford and H. F. Schaefer III, in *Reviews in Computational Chemistry* (John Wiley & Sons, Ltd, 2000) pp. 33–136.
- [10] S. Hirata, R. Podeszwa, M. Tobita, and R. J. Bartlett, *The Journal of Chemical Physics* **120**, 2581 (2004).
- [11] W. Li, Z. Yin, X. Li, D. Ma, S. Yi, Z. Zhang, C. Zou, K. Bu, M. Dai, J. Yue, Y. Chen, X. Zhang, and S. Zhang, *Scientific Reports* **14**, 16942 (2024).
- [12] M. Born and R. Oppenheimer, *Annalen der Physik* **389**, 457 (1927).
- [13] Y. Su, D. W. Berry, N. Wiebe, N. Rubin, and R. Babbush, *PRX Quantum* **2**, 040332 (2021).
- [14] R. Babbush, W. J. Huggins, D. W. Berry, S. F. Ung, A. Zhao, D. R. Reichman, H. Neven, A. D. Baczewski, and J. Lee, *Nature Communications* **14**, 4058 (2023).
- [15] J. Lee, D. W. Berry, C. Gidney, W. J. Huggins, J. R. McClean, N. Wiebe, and R. Babbush, *PRX Quantum* **2**, 030305 (2021).
- [16] W. J. Huggins, K. Wan, J. McClean, T. E. O'Brien, N. Wiebe, and R. Babbush, *Physical Review Letters* **129**, 240501 (2022), arXiv:2111.09283 [quant-ph].
- [17] A. Zhao, N. C. Rubin, and A. Miyake, *Physical Review Letters* **127**, 110504 (2021).
- [18] L. Lin, *Lecture Notes on Quantum Algorithms for Scientific Computation* (2022), arXiv:2201.08309 [quant-ph].
- [19] A. M. Childs, R. Kothari, and R. D. Somma, *SIAM Journal on Computing* **46**, 1920 (2017), arXiv:1511.02306 [quant-ph].
- [20] M. A. Nielsen and I. L. Chuang, *Quantum Computation and Quantum Information: 10th Anniversary Edition*, 1st ed. (Cambridge University Press, 2012).
- [21] T. N. Georges, M. Bothe, C. Sünderhauf, B. K. Berntson, R. Izsák, and A. V. Ivanov, *npj Quantum Information* **11**, 55 (2025).
- [22] R. Babbush, D. W. Berry, J. R. McClean, and H. Neven, *npj Quantum Information* **5**, 1 (2019).
- [23] R. Babbush, C. Gidney, D. W. Berry, N. Wiebe, J. McClean, A. Paler, A. Fowler, and H. Neven, *Physical Review X* **8**, 041015 (2018).
- [24] I. H. Kim, E. Lee, Y.-H. Liu, S. Pallister, W. Pol, and S. Roberts, *Physical Review Research* **4**, 023019 (2022), arXiv:2104.10653 [quant-ph].
- [25] H.-Y. Huang, R. Kueng, and J. Preskill, *Nature Physics* **16**, 1050 (2020).
- [26] G. H. Low, *Classical shadows of fermions with particle number symmetry* (2024), arXiv:2208.08964 [quant-ph].
- [27] B. O’Gorman, *Fermionic tomography and learning* (2022), arXiv:2207.14787 [quant-ph].
- [28] J. P. Coe, A. Moreno Carrascosa, M. Simmermacher, A. Kirrander, and M. J. Paterson, *Journal of Chemical Theory and Computation* **18**, 6690 (2022).
- [29] J. Gauss, J. F. Stanton, and R. J. Bartlett, *The Journal of Chemical Physics* **95**, 2623 (1991).
- [30] J. Gauss, J. F. Stanton, and R. J. Bartlett, *The Journal of Chemical Physics* **95**, 2639 (1991).
- [31] A. W. Harrow, A. Hassidim, and S. Lloyd, *Physical Review Letters* **103**, 150502 (2009).
- [32] Y. Tong, D. An, N. Wiebe, and L. Lin, *Physical Review A* **104**, 032422 (2021).
- [33] X. Cai, W.-H. Fang, H. Fan, and Z. Li, *Physical Review Research* **2**, 033324 (2020).
- [34] H. Chen, M. Nusspickel, J. Tilly, and G. H. Booth, *Physical Review A* **104**, 032405 (2021), arXiv:2105.01703 [quant-ph].
- [35] I. Rungger, N. Fitzpatrick, H. Chen, C. H. Alderete, H. Apel, A. Cowtan, A. Patterson, D. M. Ramo, Y. Zhu, N. H. Nguyen, E. Grant, S. Chretien, L. Wossnig, N. M. Linke, and R. Duncan, *Dynamical mean field theory algorithm and experiment on quantum computers* (2020), arXiv:1910.04735 [quant-ph].
- [36] S. Grimme, *Journal of Computational Chemistry* **27**, 1787 (2006).
- [37] S. Grimme, J. Antony, S. Ehrlich, and H. Krieg, *The Journal of Chemical Physics* **132**, 154104 (2010).
- [38] J. Lai, Y. Fan, Q. Fu, Z. Li, and J. Yang, *The Journal of Chemical Physics* **159**, 114113 (2023).
- [39] J. Tilly, H. Chen, S. Cao, D. Picozzi, K. Setia, Y. Li, E. Grant, L. Wossnig, I. Rungger, G. H. Booth, and J. Tennyson, *Physics Reports The Variational Quantum Eigensolver: A Review of Methods and Best Practices*, **986**, 1 (2022).
- [40] F. H. da Jornada, M. Lostaglio, S. Pallister, B. Şahinoğlu, and K. I. Seetharam, *A comprehensive framework to simulate real-time chemical dynamics on a fault-tolerant quantum computer* (2025), arXiv:2504.06348 [quant-ph].
- [41] L. Gao, D. Xu, H. Wan, X. Zhang, X. Dai, and L.-T. Yan, *Langmuir* **38**, 11137 (2022).
- [42] M. Von Domaros and D. J. Tobias, *Annual Review of Physical Chemistry* **76**, 231 (2025).
- [43] P. Jordan and E. Wigner, *Zeitschrift für Physik* **47**, 631 (1928).
- [44] S. B. Bravyi and A. Y. Kitaev, *Annals of Physics* **298**, 210 (2002).
- [45] J. T. Seeley, M. J. Richard, and P. J. Love, *The Journal of Chemical Physics* **137**, 224109 (2012).
- [46] S. Bravyi, J. M. Gambetta, A. Mezzacapo, and K. Temme, *Tapering off qubits to simulate fermionic Hamiltonians* (2017), arXiv:1701.08213 [quant-ph].
- [47] W. M. Kirby, S. Hadi, M. Kreshchuk, and P. J. Love, *Physical Review A* **104**, 042607 (2021).
- [48] W. Kirby, B. Fuller, C. Hadfield, and A. Mezzacapo, *PRX*

- Quantum **3**, 020351 (2022).
- [49] Y. Shee, P.-K. Tsai, C.-L. Hong, H.-C. Cheng, and H.-S. Goan, *Physical Review Research* **4**, 023154 (2022).
- [50] M. Steudtner and S. Wehner, *New Journal of Physics* **20**, 063010 (2018).
- [51] M. H. Cheng, Y.-C. Chen, Q. Wang, V. Bartsch, M. S. Kim, A. Hu, and M.-H. Hsieh, *Optimal Particle-Conserved Linear Encoding for Practical Fermionic Simulation* (2024), arXiv:2309.09370 [quant-ph].
- [52] R. Babbush, D. W. Berry, Y. R. Sanders, I. D. Kivlichan, A. Scherer, A. Y. Wei, P. J. Love, and A. Aspuru-Guzik, *Quantum Science and Technology* **3**, 015006 (2018), arXiv:1506.01029 [physics, physics:quant-ph].
- [53] J. Carolan and L. Schaeffer, *Succinct Fermion Data Structures* (2024), arXiv:2410.04015.
- [54] I. Kassal, S. P. Jordan, P. J. Love, M. Mohseni, and A. Aspuru-Guzik, *Proceedings of the National Academy of Sciences* **105**, 18681 (2008).
- [55] R. Iten, R. Colbeck, I. Kukuljan, J. Home, and M. Christandl, *Physical Review A* **93**, 032318 (2016).
- [56] R. Babbush, N. Wiebe, J. McClean, J. McClain, H. Neven, and G. K.-L. Chan, *Physical Review X* **8**, 011044 (2018).
- [57] D. Coppersmith, *An approximate Fourier transform useful in quantum factoring* (2002), arXiv:quant-ph/0201067.
- [58] L. Hales and S. Hallgren, in *Proceedings 41st Annual Symposium on Foundations of Computer Science* (IEEE Comput. Soc, Redondo Beach, CA, USA, 2000) pp. 515–525.
- [59] A. Jena, S. Genin, and M. Mosca, *Pauli Partitioning with Respect to Gate Sets* (2019), arXiv:1907.07859 [quant-ph].
- [60] T.-C. Yen, V. Verteletskyi, and A. F. Izmaylov, *Journal of Chemical Theory and Computation* **16**, 2400 (2020).
- [61] V. Verteletskyi, T.-C. Yen, and A. F. Izmaylov, *The Journal of Chemical Physics* **152**, 124114 (2020).
- [62] G. Brassard, P. Høyer, M. Mosca, and A. Tapp, in *Contemporary Mathematics*, Vol. 305, edited by S. J. Lomonaco and H. E. Brandt (American Mathematical Society, Providence, Rhode Island, 2002) pp. 53–74.
- [63] S. Aaronson, *SIAM Journal on Computing* **49**, STOC18 (2020).
- [64] H.-Y. Huang, R. Kueng, and J. Preskill, *Physical Review Letters* **126**, 190505 (2021).
- [65] L. Lin and Y. Tong, *Quantum* (2020).
- [66] Y. Ge, J. Tura, and J. I. Cirac, *Journal of Mathematical Physics* **60**, 022202 (2019).
- [67] J. W. Negele and H. Orland, *Quantum Many-Particle Systems*, *Frontiers in Physics* No. 68 (Addison-Wesley Pub. Co, Redwood City, Calif, 1988).
- [68] R. M. Martin, L. Reining, and D. Ceperley, *Interacting Electrons: Theory and Computational Approaches* (Cambridge University Press, New York, NY, 2016).
- [69] R. P. Feynman, *Physical Review* **56**, 340 (8).
- [70] D. W. Berry, C. Gidney, M. Motta, J. R. McClean, and R. Babbush, *Quantum* 10.22331/q-2019-12-02-208 (2019).
- [71] V. Von Burg, G. H. Low, T. Häner, D. S. Steiger, M. Reiher, M. Roetteler, and M. Troyer, *Physical Review Research* **3**, 033055 (2021).
- [72] D. W. Berry, M. Kieferová, A. Scherer, Y. R. Sanders, G. H. Low, N. Wiebe, C. Gidney, and R. Babbush, *npj Quantum Information* **4**, 22 (2018).
- [73] E. Malveti, R. Iten, and R. Colbeck, *Quantum Circuits for Sparse Isometries* (2021), arXiv:2006.00016.
- [74] P. Giannozzi, S. Baroni, N. Bonini, M. Calandra, R. Car, C. Cavazzoni, D. Ceresoli, G. L. Chiarotti, M. Cococcioni, I. Dabo, A. D. Corso, S. de Gironcoli, S. Fabris, G. Fratesi, R. Gebauer, U. Gerstmann, C. Gougoussis, A. Kokalj, M. Lazzeri, L. Martin-Samos, N. Marzari, F. Mauri, R. Mazzarello, S. Paolini, A. Pasquarello, L. Paulatto, C. Sbraccia, S. Scandolo, G. Sclauzero, A. P. Seitsonen, A. Smogunov, P. Umari, and R. M. Wentzcovitch, *Journal of Physics: Condensed Matter* **21**, 395502 (2009).
- [75] P. Giannozzi, O. Andreussi, T. Brumme, O. Bunau, M. B. Nardelli, M. Calandra, R. Car, C. Cavazzoni, D. Ceresoli, M. Cococcioni, N. Colonna, I. Carnimeo, A. D. Corso, S. de Gironcoli, P. Delugas, R. A. DiStasio, A. Ferretti, A. Floris, G. Fratesi, G. Fugallo, R. Gebauer, U. Gerstmann, F. Giustino, T. Gorni, J. Jia, M. Kawamura, H.-Y. Ko, A. Kokalj, E. Küçükbenli, M. Lazzeri, M. Marsili, N. Marzari, F. Mauri, N. L. Nguyen, H.-V. Nguyen, A. Otero-de-la-Roza, L. Paulatto, S. Poncé, D. Rocca, R. Sabatini, B. Santra, M. Schlipf, A. P. Seitsonen, A. Smogunov, I. Timrov, T. Thonhauser, P. Umari, N. Vast, X. Wu, and S. Baroni, *Journal of Physics: Condensed Matter* **29**, 465901 (2017).
- [76] R. M. Martin, *Electronic Structure: Basic Theory and Practical Methods*, 1st ed. (Cambridge University Press, 2004).

Supporting Information for “Optimizing Quantum Chemistry Simulations with a Hybrid Quantization Scheme”

Appendix A.1: Summary of mentioned encodings

1. First-Quantized Encoding

The first-quantized representation uses the tensor products of the single-particle wavefunctions ψ_1, \dots, ψ_N , called Hartree products, as a basis. Since a single Hartree product does not obey the Pauli exclusion principle, fermionic antisymmetry is enforced by explicitly expressing the wavefunction as a linear combination of Hartree products, forming a Slater determinant. This can be represented as a matrix determinant with $N!$ terms.

$$[\psi_1, \dots, \psi_N] = \frac{1}{\sqrt{N!}} \begin{vmatrix} \psi_1(\mathbf{x}_1) & \cdots & \psi_N(\mathbf{x}_1) \\ \vdots & \ddots & \vdots \\ \psi_1(\mathbf{x}_N) & \cdots & \psi_N(\mathbf{x}_N) \end{vmatrix}$$

Slater determinants serve as the basis for the second-quantized representation, while the Hartree products are used as the basis for the first-quantized representation. The first-quantized encoding [13, 22] encodes a single Hartree product as follows.

$$\begin{aligned} \Psi &= \psi_{i_1}(\mathbf{x}_1) \otimes \psi_{i_2}(\mathbf{x}_2) \otimes \cdots \otimes \psi_{i_n}(\mathbf{x}_n) \\ \mathcal{E}(\Psi) &= |i_1\rangle \otimes |i_2\rangle \otimes \cdots \otimes |i_n\rangle \end{aligned}$$

Here, $|i_1\rangle, \dots, |i_n\rangle \in \{|1\rangle, \dots, |M\rangle\}$ are binary representations of indices to the single-particle basis $|\psi_1(\mathbf{x})\rangle, \dots, |\psi_M(\mathbf{x})\rangle$, each encoded in $\lceil \log_2 M \rceil$ qubits for N electrons, totalling $N \lceil \log_2 M \rceil$ qubits. Unlike the sorted-list encoding, the indices are not sorted, as different orderings correspond to distinct Hartree products. The antisymmetrization of the wavefunction here must be performed explicitly during the quantum simulation process, primarily during state initialization [22]. Hamiltonian simulation preserves this antisymmetry as long as the input wavefunction is symmetric, eliminating the need for continuous antisymmetrization.

2. Sorted-List Encoding

The sorted-list encoding is first proposed by Carolan and Schaeffer [53]. While they introduced several variants of the $\mathcal{O}(N \log M)$ second-quantized encodings, we only used the variant detailed in Section 4.2 of their paper, which we termed the sorted-list encoding. This variant has the simplest encoding along with the most efficient circuit implementations in terms of gate count, while others increase the complexity of the circuit implementations to save either the qubit count and/or the circuit depth. This variant also allows us to create efficient conversions between the first-quantized and second-quantized encodings.

Let $\mathbf{x} \in \mathbb{F}_2^M$ be the bitstring representing a Slater determinant with Hamming weight $|\mathbf{x}| = N$, indicating N electrons. We then define $\mathbf{e}_i \in \mathbb{F}_2^M$ to be a bitstring with a ‘1’ in position i and ‘0’ elsewhere. Thus, $\mathbf{x} = \mathbf{e}_{i_1} \oplus \mathbf{e}_{i_2} \oplus \cdots \oplus \mathbf{e}_{i_N}$ with $i_1 < i_2 < \cdots < i_N$. The sorted-list encoding \mathcal{E} concatenates the binary representation of each of the occupied orbital indices in ascending order.

$$\mathcal{E}(\mathbf{x}) = |i_1\rangle \otimes |i_2\rangle \otimes \cdots \otimes |i_N\rangle \otimes |\infty\rangle \otimes \cdots \otimes |\infty\rangle$$

Each orbital index $|i\rangle$ is encoded as a binary string of $\lceil \log_2 M \rceil$ qubits. The number of registers N_{reg} does not need to equal to the number of electrons N . To support particle non-conserving operations, a sentinel state, representing an “unoccupied” orbital, is used to fill in the empty registers when $N < N_{\text{reg}}$. By convention, the sentinel state is represented by the symbol $|\infty\rangle$ and is ordered greater than all orbital indices. Thus, $N_{\text{reg}} \lceil \log_2(M+1) \rceil$ qubits can hold all bitstrings with Hamming weight less than or equal to N_{reg} . This enables the sorted-list encoding to perform particle non-conserving operations as long as enough registers are set aside for the operation.

Before elaborating how fermionic operations are encoded, we first introduce several building block gates frequently used in the sorted-list encoding. The $= p$ gate (Figure A.5) accepts one register as input and flips a target ancilla qubit if that register is equal to p . Similarly, the $< p$ gate (Figure A.6) accepts one register as input and flips a target ancilla qubit if that register is less than p . The bubble gate U_p (Figure A.7) accepts two registers as input and swaps

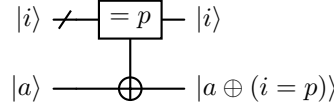


Figure A.5. The $= p$ circuit [53]. This circuit flips t when the value of i is equal to a constant p .

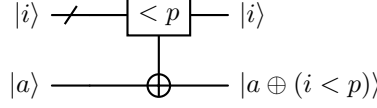


Figure A.6. The $< p$ circuit [53]. This circuit flips t when the value of a is less than a constant p . While the figure above shows the $< p$ gate, the original work includes the $\leq p$ and $> p$ variant which can be implemented similarly [70].

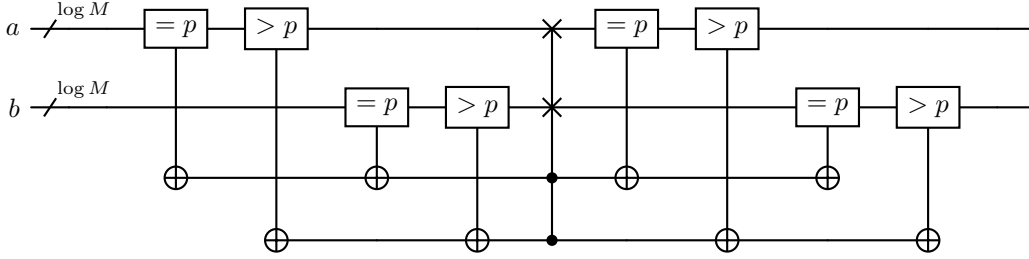


Figure A.7. The bubble circuit U_p [53]. This circuit swaps the two registers a and b when one of them is equal to p and the other is larger than p . The $= p$ circuit is simply the $\log M$ qubit Toffoli gate while the $> p$ gate can be adapted from Figure A.6.

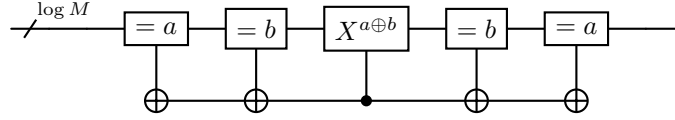


Figure A.8. The $a \leftrightarrow b$ circuit [53]. This circuit outputs b when the input is a and outputs a when the input is b . Otherwise, the input is unchanged. The $X^{a \oplus b}$ is composed of multiple CNOT gate according to the binary representation of $a \oplus b$.

the two registers if one of them is equal to p and the other is larger than p . Finally, the $a \leftrightarrow b$ (Figure A.8) gate outputs b when the input is a and outputs a when the input is b . Otherwise the input remains unchanged.

Fermionic operations on this encoding are first decomposed to Majorana operators. The Majorana operators are then further decomposed to sgn-rank and bit-flip operators.

$$\begin{aligned}
 a_p^\dagger &= \frac{1}{2}(\gamma_{2p-1} - i\gamma_{2p}) & a_p &= \frac{1}{2}(\gamma_{2p-1} + i\gamma_{2p}) \\
 \mathcal{E}(\gamma_{2p-1}) &= \text{bit-flip}(p) \text{sgn-rank}(p-1) & \mathcal{E}(\gamma_{2p}) &= i \text{bit-flip}(p) \text{sgn-rank}(p)
 \end{aligned}$$

The $\text{sgn-rank}(p)$ operator calculates the parity of the number of occupied states for orbital indices less than or equal to p . It then multiplies the wavefunction by -1 for odd parity and $+1$ for even parity. On the other hand, the $\text{bit-flip}(p)$ operator flips the occupation of orbital p . The circuit implementations of the sgn-rank and bit-flip operators can be found in Figure A.9 and A.10, respectively. Essentially, the $\text{sgn-rank}(j)$ circuit applies a Z gate for every register containing an orbital index less than or equal to j . On the other hand, $\text{bit-flip}(j)$ first checks if j is occupied. If j is occupied it replaces $|j\rangle$ with $|\infty\rangle$, otherwise it replaces $|\infty\rangle$ with $|j\rangle$. After replacing the target register with the appropriate value, that register is sorted back to the correct ascending order. As the Majorana operators changes the number of occupied orbitals, the encoding needs to set aside more registers than the total number of electrons. More specifically, the one-electron terms will require 2 extra registers in the encoding than the total number of electrons, while the two-electron terms will require 4 extra registers. Such registers are filled with the $|\infty\rangle$ state so that the swap circuit in Figure A.10 can be done.

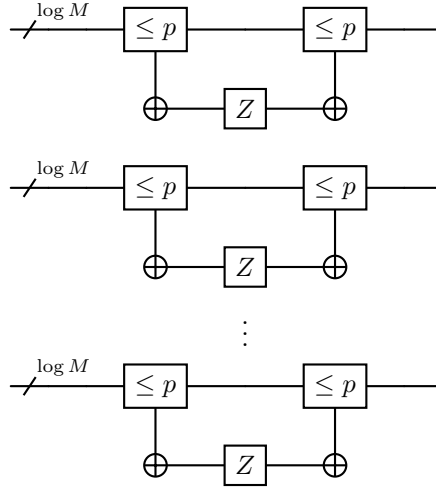


Figure A.9. The $\text{sgn-rank}(p)$ circuit [53]. The $\leq p$ circuit is shown on Figure A.6. Quantum wires not extending to both ends of the circuit are ancilla qubits.

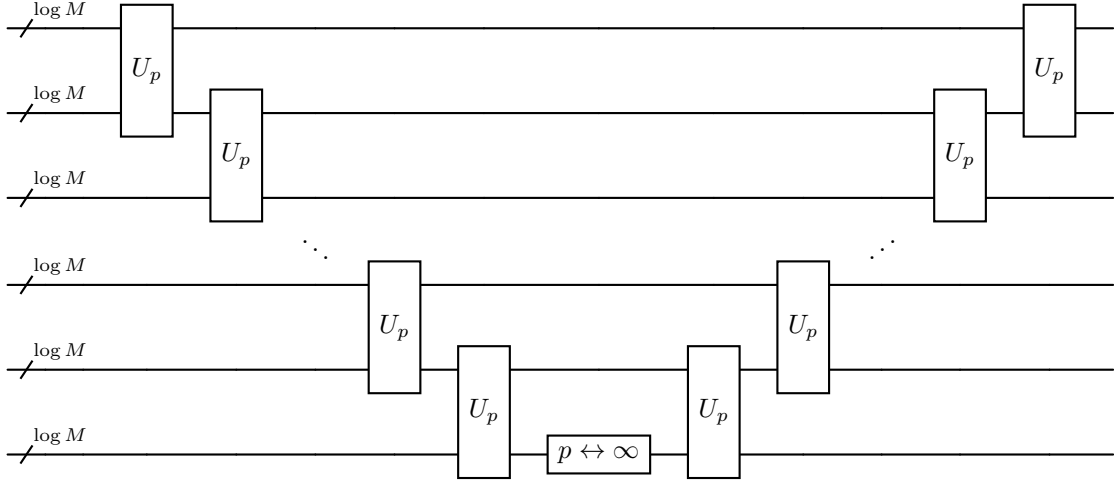


Figure A.10. The $\text{bit-flip}(p)$ circuit [53]. The bubble circuit U_p is shown on Figure A.7, while the swap circuit $p \leftrightarrow \infty$ is shown in Figure A.8.

Appendix A.2: Simulation Details for the Fe_2O_3 Surface Calculation

We performed the DFT calculation of the Fe_2O_3 (01 $\bar{1}$ 2) surface with a benzene molecule, using the plane-wave code Quantum Espresso [74, 75]. For the Fe_2O_3 (01 $\bar{1}$ 2) surface, we prepared a $15.07 \text{ \AA} \times 16.28 \text{ \AA} \times 5.65 \text{ \AA}$ system with the norm-conserving pseudopotential and a wavefunction cut-off of 80 Ry. Furthermore, a DFT+U correction of 5.0 eV was applied to the Fe-3d orbitals. Geometry optimizations were conducted at varying simulation cell heights (z axis), achieving convergence in the DFT energies for a simulation cell height of 14 \AA . We then placed a benzene molecule midway between the surface and its periodic image, and performed geometry optimisations at different simulation cell heights. In this case, convergence in DFT energies was achieved for a simulation cell height of 23 \AA , implying an extra 9 \AA of vacuum space to create unentangled ground states. Both of these are shown in Figure 4 of the main manuscript.

The 9 \AA vacuum space corresponds to approximately $\sim 6.5 \times 10^5$ additional plane-waves. To confirm that the extra vacuum space creates unentangled ground states, we performed an isolated benzene calculation with the same parameters and vacuum space as the isolated Fe_2O_3 surface. The difference in DFT energies between the isolated and the combined systems was 0.899 mRy, well below chemical accuracy.

It is important to note that the plane-wave cut-offs for the many-body quantum simulation are significantly higher than those for DFT, as the use of pseudopotentials and the approximate exchange-correlation functionals reduce the need for high-frequency wavevectors in DFT. Furthermore, errors due to the divergence of the coulomb terms are also minimized in DFT as long as the simulation cell is neutral [76].

Appendix A.3: Details on the Green's function calculation

Here, we use the preconditioned fast inversion algorithm [32]. To estimate the cost for the first-quantized plane-wave Hamiltonian, we follow Theorem 2 of that paper. We can take the kinetic terms as U_A and the external potential and Coulomb terms as U_B , with the 1-norm scaling as $\lambda_A = \mathcal{O}(NM^{2/3}/\Omega^{2/3})$ and $\lambda_B = \mathcal{O}(N^2M^{1/3}/\Omega^{1/3})$ [13], respectively. As a result, we can obtain a block-encoding of $(z \pm [H - E_0])^{-1}$ for some $\eta \geq |z|$ using

$$\begin{aligned} \mathcal{O}\left(\frac{\lambda_B}{\tilde{\sigma}_{\min}^2 \varepsilon} \ln\left(\frac{1}{\varepsilon \tilde{\sigma}_{\min}}\right) \ln\left(\frac{1}{\delta}\right)\right) &= \mathcal{O}\left(\frac{\lambda_B^3}{\eta^2 \varepsilon} \ln\left(\frac{1}{\delta}\right)\right) \\ &= \mathcal{O}\left(\frac{N^6 M}{\Omega \eta^2 \varepsilon} \ln\left(\frac{1}{\delta}\right)\right) \end{aligned}$$

applications of U'_A and U_B , using the worst-case bound of $\tilde{\sigma}_{\min} = \eta/(1 + \eta + \lambda_B)$.

On the other hand, a block-encoding of $(z \pm [H - E_0])^{-1}$ for some $\eta \geq |z|$ using the non-preconditioned inversion method [19] requires

$$\mathcal{O}\left(\frac{\lambda}{\eta^2 \varepsilon}\right) = \mathcal{O}\left(\frac{NM^{2/3}}{\Omega^{2/3} \eta^2 \varepsilon} + \frac{N^2 M^{1/3}}{\Omega^{1/3} \eta^2 \varepsilon}\right)$$

applications of the qubitization circuits, with $\lambda = \lambda_A + \lambda_B$.